J. Marine Sci. Appl. (2016) 15: 157-165
DOI: 10.1007/s11804-016-1348-8

Three-Dimensional Numerical Investigation of the Separation Process in a Vortex Tube at Different Operating Conditions

Seyed Ehsan Rafiee* **and M. M. Sadeghiazad**

Department of Mechanical Engineering, Urmia University of Technology, Urmia P.O. Box 57155-419, Iran

Abstract: Air separators provide safe, clean, and appropriate air flow to engines and are widely used in vehicles with large engines such as ships and submarines. In this operational study, the separation process in a Ranque–Hilsch vortex tube cleaning (cooling) system is investigated to analyze the impact of the operating gas type on the vortex tube performance; the operating gases used are air, nitrogen, oxygen, carbon dioxide and nitrogen dioxide. The computational fluid dynamic model used is equipped with a three-dimensional structure, and the steady-state condition is applied during computations. The standard k–ε turbulence model is employed to resolve nonlinear flow equations, and various key parameters, such as hot and cold exhaust thermal drops, and power separation rates, are described numerically. The results show that nitrogen dioxide creates the greatest separation power out of all gases tested, and the numerical results are validated by good agreement with available experimental data. In addition, a comparison is made between the use of two different boundary conditions, the pressure-far-field and the pressure-outlet, when analyzing complex turbulent flows in the air separators. Results present a comprehensive and practical solution for use in future numerical studies.

Keywords: vortex tube, air separator, separation process, operating gas, numerical simulation

Article ID: 1671-9433(2016)02-0157-09

1 Introduction

A vortex tube is an uncomplicated device with no moving parts that separates a pressurized operating fluid in two different streams, dirty and clean (or hot and cold). The separator system contains a vortex chamber, several slots, a cold orifice, a working tube, and a conical valve. In the air separator, the super rotational flow field occurs at 10^6 r/min. When a fluid (which is compressed by a compressor) enters the air separator via the nozzles (slots), a powerful turbulent field is created during tangential movement in the main tube. The center of the vortex tube can be regarded as the axis of the rotation, and it can be said that the operating gas expands and temperature drops when the pressurized gas layers are turning tangentially around this center. Thus, separation occurs during the rotational movement of the fluid layers, and the pressurized gas is divided in two flows, namely clean (cold) and dirty (hot) flows. An orifice exists near the nozzles within the vortex tube cooling or cleaning systems, and the cold flow is extracted through this from the cooling system. The rate of clean or cold flow is controlled by a conical or throttle valve located on the hot side, which controls the flow of cold air through the warm air flow. The vortex tube air separator was invented by Ranque (1933), a French researcher, and it was then geometrically improved by Hilsch (1947). However, although a large amount of research has been conducted on vortex tube air separators, the details of the separation process occurring in the vortex tube air separator have not yet been explained to date, and thus, in this article, we utilize numerical models to clarify this. A brief list of previous important work is presented below.

Dutta *et al*. (2011) used a National Institute of Standards and Technology (NIST) real gas model (as a CFD model) to investigate the flow pattern in an air separator. The capabilities of different turbulence models (RSM, LES, k–ω, k–ε, and SST k–ω) in predicting flow structures in an air separator were examined by Baghdad *et al*. (2011) and Rafiee and Sadeghiazad (2016). Variations in temperature drops are seen when a bended main tube is used in the structure of an air separator, and these were reported using a comparison with an air separator equipped a straight main tube by Rafiee *et al*. (2016), Bovand *et al*. (2014a, 2014b), and Valipour and Niazi (2011). Skye *et al*. (2006) initially performed experimental work on the thermal and flow separation in a commercial vortex tube, and Dincer *et al*. (2011) adjusted the three classifications of vortex tubes: (a) a six cascade-type RHVT, (b) vortex tube with a threefold cascade situation, and (c) conventional vortex tube. The effect of a divergent main tube was investigated by Rahimi *et al*. (2013), and the optimum angle for the divergent main tube was achieved numerically. In addition, various factors relating to the vortex tube structure (inlet slots, ratio of slots, hot and cold exit area, rounding-off edge radius, internal radius of main tube, and convergent slots) were optimized by Rafiee and Sadeghiazad (2015), Rafiee *et al*. (2013), Pourmahmoud *et al*. (2012), and Im and Yu (2012). A number of refrigerant gases (R728, R32, R134a, R161, R744, and R22) were also examined in the

Received date: 2015-12-03
Accepted date: 2016-01-14
***Corresponding author Email:** s.e.rafiee@mee.uut.ac.ir

vortex tube air separator; the thermal performance of the air separator was studied and the optimum refrigerant gas determined (Pourmahmoud *et al*., 2013; Han *et al*., 2013). This effect was also studied by Thakare and Parekh (2015) using various viewpoints and different gases. Mohammadi and Farhadi (2013) conducted a laboratory study the optimization of the nozzle diameter and the cold flow fraction, and Rafiee and Sadeghiazad (2014a, 2014b) performed experimental setups to optimize the control valve structural parameters, such as the conical angle and cone length, and proved that certain optimized values lead to the best thermal capability. Some researchers have stated that a higher thermal ability is achieved with a larger number of nozzles (Shamsoddini and Hossein Nezhad, 2010). In addition, it has been determined that the nozzle shape can be a strong and effective parameter affecting the cooling ability or the heating effectiveness of the air separator. Convergent nozzles (as a new shape) were examined and optimized by Rafiee and Rahimi (2013), and the impact of a hot tube with a new shape (convergent main tube) was then experimentally tested by Rafiee *et al*. (2015). These results determined the use of an optimal angle for the convergent main tube to produce the best cooling capacity. Xue *et al*. (2013a) and Rafiee and Sadeghiazad (2014c) proposed a new energy explanation when analyzing the thermal distribution and exergy density in the air separator by applying measured flow factors along the hot tube. Optimization work was performed by Xue *et al*. (2013b) on the impact of the cold flow fraction; this study focused on an equal share of the rotating flows between the hot and cold exhausts. Finally, thermophysical parameters (total temperature, total pressure, and tangential velocity) in the vortex tube were comprehensively reported by Rafiee and Rahimi (2014), and the influence of inlet temperature on vortex tube performance was investigated by Pourmahmoud *et al*. (2014).

The main aim of this study is to determine both the advantage of utilizing the best operating gas (for cooling or heating) and its clear role in improving the thermal capacity of the air separator. We thus aim to select the best operating gas for delivering optimum cooling and heating capabilities.

2 Governing equations

The important parameters within the system are as follows:

$$\alpha = \frac{\dot{m}_c}{\dot{m}_i} \tag{1}$$

where α is the cold flow fraction, and $\dot{m}_c$ and $\dot{m}_i$ are the cold flow rate and the rate of the inlet gas, respectively.

The extremely rotating and compressible flow field in the air separator is considered as the main computational domain in the creation of a three-dimensional structure. In addition, a commercial code (Fluent 6.3.26) is employed to simulate the turbulent patterns in the air separator using the standard k–ε turbulence model. Turbulence models, such as RSM and LES, are very accurate (for rotational issues), but as the CPU time is very large in these models, a model is selected that is affordable in terms of accuracy and CPU time. In addition, it has previously been determined in a considerable amount of research, that the standard k–ε is an affordable turbulence model (time and precision) and its results have acceptable accuracy when validating experimental results (Rafiee *et al*., 2013). The developed numerical model is restricted by the following considerations: (a) constant operating fluid properties; (b) assumption of a fully turbulent flow field regime; (c) consideration of the steady-state condition. Using these conditions and assumptions, we present the governing equations as continuity (conservation of mass), momentum, and energy equations, which can be written respectively as

$$\frac{\partial}{\partial x_j}(\rho u_j) = 0 \tag{2}$$

$$\frac{\partial}{\partial x_j}(\rho u_i u_j) = -\frac{\partial p}{\partial x_i} + \frac{\partial}{\partial x_j}\left[\mu\left(\frac{\partial u_i}{\partial x_j} + \frac{\partial u_j}{\partial x_i} - \frac{2}{3}\delta_{ij}\frac{\partial u_k}{\partial x_k}\right)\right] + \frac{\partial}{\partial x_j}(-\overline{\rho u_i' u_j'}) \tag{3}$$

$$\frac{\partial}{\partial x_i}\left[u_i\rho\left(\frac{1}{2}u_j u_j + h\right)\right] = \frac{\partial}{\partial x_j}\left[u_i(\tau_{ij})_{\text{eff}} + k_{\text{eff}}\frac{\partial T}{\partial x_j}\right] \tag{4}$$

$$k_{\text{eff}} = \frac{c_p \mu_t}{Pr_t} + K$$

where Pr is the Prandtl number. One of the assumptions used to simplify the heat transfer computations is that the operating fluid is considered as an ideal gas. The compressibility effect is thus inherent as

$$p = \rho RT \tag{5}$$

Eqs. (6) and (7) present the detailed configurations of the dissipation rate (ε) and turbulence kinetic energy (k) in relation to the standard k–ε turbulence model:

$$\frac{\partial}{\partial t}(\rho\varepsilon) + \frac{\partial}{\partial x_i}(\rho\varepsilon u_i) = \frac{\partial}{\partial x_j}[(\mu + \frac{\mu_t}{\sigma_\varepsilon})\frac{\partial \varepsilon}{\partial x_j}] + C_{1\varepsilon}\frac{\varepsilon}{k}(G_k + C_{3\varepsilon}G_b) - C_{2\varepsilon}\rho\frac{\varepsilon^2}{k} \tag{6}$$

$$\frac{\partial}{\partial t}(\rho k) + \frac{\partial}{\partial x_i}(\rho k u_i) = \frac{\partial}{\partial x_j}[(\mu + \frac{\mu_t}{\sigma_k})\frac{\partial k}{\partial x_j}] + G_k + G_b - \rho\varepsilon - Y_M \tag{7}$$

where G_k and G_b are turbulence kinetic energy generation regarding the gradients of mean velocity and buoyancy effect, respectively; Y_M is the fluctuating stretch contribution in compressible turbulence to the overall rate of dissipation; $C_{1\varepsilon}$ and $C_{2\varepsilon}$ are two constants; and σ_ε and σ_k are Prandtl numbers (turbulent). The constants in Eqs. (6) and (7) are σ_ε=1.3, $C_{1\varepsilon}$=1.44, $C_{2\varepsilon}$=1.92, C_μ=0.09, σ_k=1.0, and σ_ε=1.3. Turbulent viscosity μ_t can then be defined as

$$\mu_t = \rho C_\mu \frac{k^2}{\varepsilon} \tag{8}$$

where C_μ=0.09 and is a constant value.

3 Description of the physical model

3.1 Three-dimensional CFD model

The separation process occurring in a vortex tube air separator is simplified and shown in Fig. 1.

A three-dimensional model of an air separator is created and developed based on the experimental air separator cooling system used by Skye *et al*. (2006), where the model of the vortex tube air separator used was the Exair™ 708 slpm. Fig. 2 shows a schematic representation of this model, and the structural dimensions of the air separator are summarized in Table 1. Fig. 3(a) shows the computational grids created, where it can be seen that the created CFD model of the air separator uses a structured grid pattern to divide the domain in cubic units (with the exception of volume units around the center line that are triangular prism units). The reasons for this are that calculations of a domain that has an unstructured mesh grid system usually involve more CPU time than the calculations of a domain with a structured mesh grid arrangement. In addition, structured arrangements are more accurate than unstructured ones.

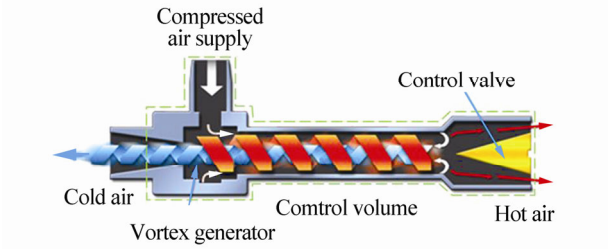

Fig. 1 Simplified diagram of vortex tube structure and separation process

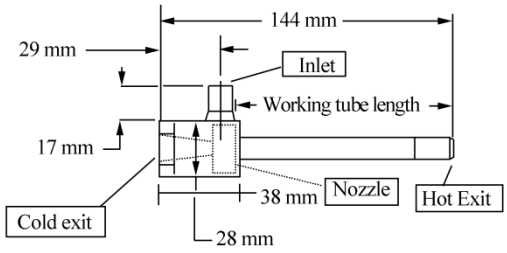

Fig. 2 Diagram of air separator structure as used in tests

Table 1 Geometrical details of CFD models that are similar to those of experimental dimensions

Structural parameter	Value
Area of hot exit/mm^2	95
Diameter of hot exit/mm	11
Diameter of cold exhaust/mm	6.2
Slot area/mm^2	8.2
Width of nozzle/mm	1.41
Area of cold exit/mm^2	30.3
Height of nozzle/mm	0.97
Diameter of main tube/mm	11.4
Length of main tube/mm	106

The velocity pressure coupling in computations uses the SIMPLE algorithm, and the convective items are discretized using the second-order upwind scheme. For the energy terms, the minimum value of the convergence standard for the turbulence and velocity quantities and the continuity equation were 10^{-6} and 10^{-13}, respectively.

One of the advantages of the CFD model created is that the hot control valve is modeled completely (as seen in Fig.3(b)), which thus enables real modeling of the flow pattern in the air separator as much as possible. The flow field in the air separator is extremely complex, and thus, a number of special combinations of relaxation factors are used to simulate the separation process occurring in the device. The ranges of relaxation factors are presented as follows: pressure (0.1–0.2), density (0.1–1), body force (0.1–1), momentum (0.1–0.6), and energy (0.1–1). As shown in Fig. 3(c), for a greater accuracy, this CFD model has fine mesh grids close to the cold and hot exhausts to enable the accurate measurement of cold and hot temperatures in these areas.

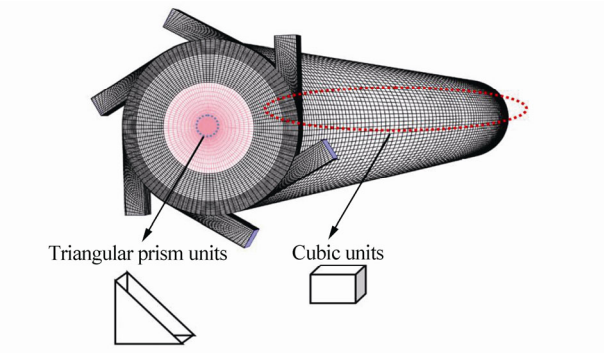

(a) Mesh arrangement of CFD model

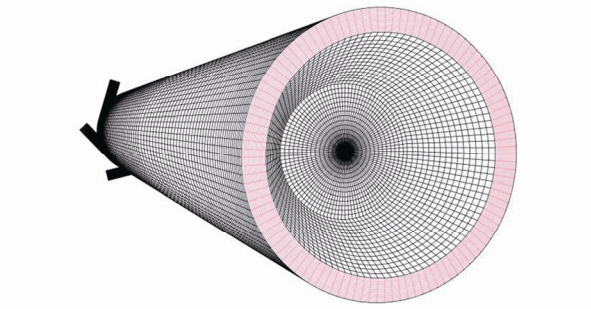

(b) End view of CFD model (hot control valve side)

(c) Longitudinal arrangement of mesh grids

Fig. 3 Three-dimensional CFD modeling

3.2 Grid independence study, boundary conditions, and validation

A careful analysis of the grid-independence process of CFD computations is performed to determine the validity

and accuracy of CFD outputs. 3D CFD models that are based on various average unit cell volumes are created during the grid-independence test, and in this respect four grid systems are created and analyzed to consider the most accurate grid numbers for use in the CFD models. Thermal and velocity investigations are performed for four different average unit cell volumes. The optimum cold flow fraction at which the highest cooling power can be found is 0.3, and thus an independence study is conducted at this cold flow fraction (α=0.3). Variations of two main parameters, maximum tangential velocity and the cold exit temperature difference, are considered for different unit cell volumes, as shown in Figs. 4 and 5. It can be seen that applying numerical models with average unit cell volumes that are smaller than 0.025 7 mm^3 (corresponding to 287 000 cells) has no significant effect on the results. Therefore, the use of 287 000 cells is considered to present both accuracy and efficiency and is thus applied in all models within this study.

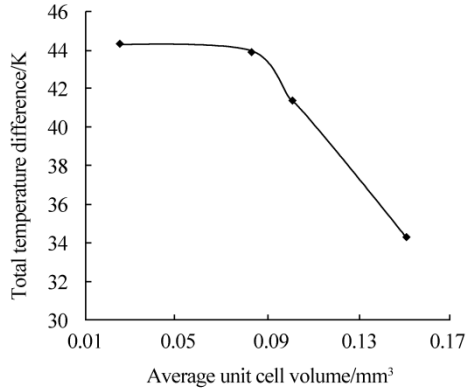

Fig. 4 Grid independence analysis of total temperature difference

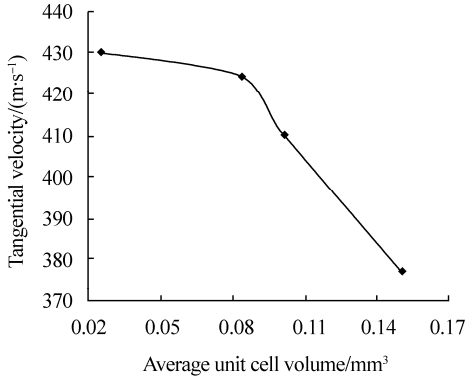

Fig. 5 Grid independence analysis of maximum swirl velocity

Fig. 6 shows a schematic diagram of the boundary conditions used in the vortex tube air separator CFD model. The mass-flow-inlet boundary condition is considered for the injectors, with a mass flow rate of 8.35 g/s (4.8 bar), and temperature at the slots is adjusted to an ambient temperature of 294.2 K (based on experimental data). The no-slip situation is also applied for the walls of the air separator. There are two types of boundary conditions that can be used at the slot surfaces, namely the pressure-far-field and the pressure-outlet. When performing computations during experiments, researchers use the pressure-outlet boundary condition to measure the pressure values at cold and hot exhausts, and this method is thus applicable for those who have access to laboratory data.

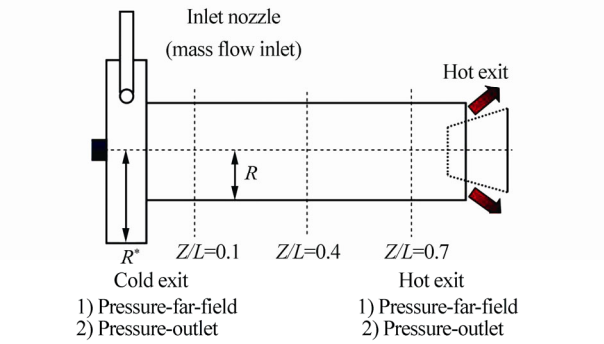

Fig. 6 Details of boundary conditions used in computations

For the pressure inlet boundary condition in the case of a vortex tube, the regime of flow in the domain can be assumed to be a compressible flow, and thus isentropic equations for gas with an ideal condition are employed for static pressure, total pressure, and velocity at the pressure inlet boundary. Total pressure (p_0') and static pressure (p_s') are determined using the following equations:

$$\frac{p_0' + p_{op}}{p_0' + p_{op}} = (1 + \frac{\gamma - 1}{2} M^2)^{\frac{\gamma}{\gamma - 1}} \tag{9}$$

and

$$M \equiv \frac{v}{c} = \frac{v}{\sqrt{\gamma R T_s}} \tag{10}$$

where c is the sound speed and $\gamma = \frac{C_p}{C_v}$. It should also be said that p_{op} (operating pressure) is included in Eq. (9) because our boundary condition inputs are defined as a function of pressure relative to operating pressure.

On the basis of introducing Riemann details for a one-dimensional pattern normal to boundary, the pressure far-field boundary condition can be defined as a boundary condition with a non-reflecting situation. Two Riemann details (invariants) for a subsonic flow exist, which correspond to outgoing and incoming waves,

$$R_\infty = v_{n\infty} - \frac{2c_\infty}{\gamma - 1} \tag{11}$$

$$R_i = v_{ni} - \frac{2c_i}{\gamma - 1} \tag{12}$$

where v_n is defined as the magnitude of velocity normal to the boundary, c is the local sound speed, and γ is the specific

heat ratio for an ideal gas. The subscript ∞, corresponds to the conditions at infinity, and *i* corresponds to the domain interior. Therefore, these two invariants can be defined as

$$v_n = \frac{1}{2}(R_i + R_\infty) \tag{13}$$

$$c = \frac{\gamma - 1}{4}(R_i - R_\infty) \tag{14}$$

And v_n becomes the normal velocity value on the boundary. In this study, we introduce a boundary condition method that can be used by researchers that have no access to laboratory data; in other words, this article introduces a simple way of analyzing a real model of the air separator where the pressure values at exhausts are unknown. Pressure values are not required when the model is created based on pressure-far-field boundary conditions. However, it is thus necessary to prove that the results of the two methods (pressure-far-field and pressure-outlet) are consistent with each other.

In the CFD model of the vortex tube air separator, the cold flow fraction is altered to achieve different efficiency levels with both the pressure-far-field and the pressure-outlet, and the procedure used to achieve this during application of these different boundary conditions is as follows:

a) For the pressure-outlet, we consider a fixed pressure value at the cold outlet and change the pressure at the hot outlet (as the experimental values).

b) For the pressure-far-field we adjust the constant cold exit area and vary the hot area.

c) For the experimental model, we control the valve performance.

It can thus be seen that using the second mode (pressure-far-field) delivers results that are closest to the experimental process. Figs. 7 and 8 show a comparison of the boundary conditions, where a comparison between the numerical outputs (cold and hot temperatures resulting from both boundary conditions) and the experimental results of Skye *et al*. (2006) are compared. It can be seen from Table 1, that all the structural factors in both the real and CFD models are the same and that the only difference between the CFD models is the type of boundary condition used and that the operating conditions are adjusted as real conditions. The main difference between the computational and real models is that the adiabatic boundary condition is applied to the main tube wall (the outer surface), and the convection heat transfer between the air separator and the environment is neglected. As depicted in Figs. 7 and 8, the results of 3D computations (for both boundary conditions) are in agreement with the experimental outputs from the real model. All the predicted values are within 7% of the laboratory results, which is an acceptable range. Figs. 7 and 8 show the developed model to be an accurate model that creates reliable results using either types of boundary condition (i.e., pressure-far-field or pressure-outlet).

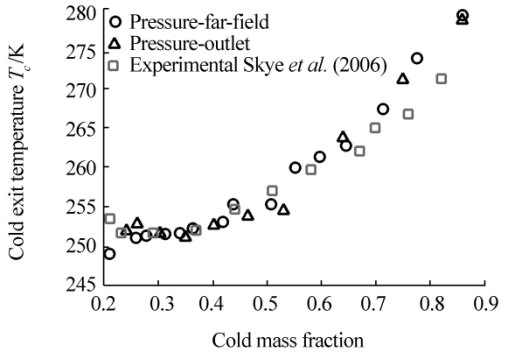

Fig. 7 Experimental cold exit temperature compared with numerical values from 3D CFD models applying both types of boundary conditions

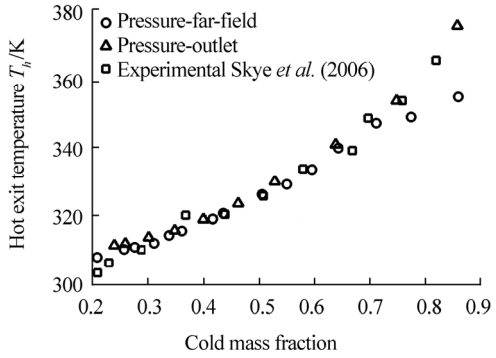

Fig. 8 Experimental hot exit temperature compared with numerical values from 3D CFD models applying both types of boundary conditions

To present a complete comparison between pressure-far-field and pressure-outlet boundary conditions, a number of parameters are studied as a function of *r*/*R* (dimensionless radial distance), such as axial velocity, tangential velocity, total pressure and total temperature at three different longitudinal sections (*Z*/*L*=0.1, 0.4, and 0.7 as Fig. 6) of the working tube, and total temperature on the wall of the vortex tube air separator. Axial and rotational velocities and total pressure and temperature distributions in different axial sections are shown in Figs. 9–12; these illustrate a comparative presentation of CFD results when employing two different boundary conditions, and show the good adjustability of results for both models.

Fig. 13 shows a comparison of total temperature variations on the wall of the tube for both boundary conditions (pressure-far-field and pressure-outlet), where good agreement between both CFD models can be seen. Figs. 9–13 show that both boundary conditions deliver almost identical results, and thus either can be used during the numerical process. However, it is considered that the pressure-far-field boundary condition is more usable than the other condition, because there is no access to the pressure values of the exhausts in most cases, and this method does not require knowledge of the outlet pressure. Therefore, in the remainder of this study, the

pressure-far-field boundary condition is applied in all numerical computations.

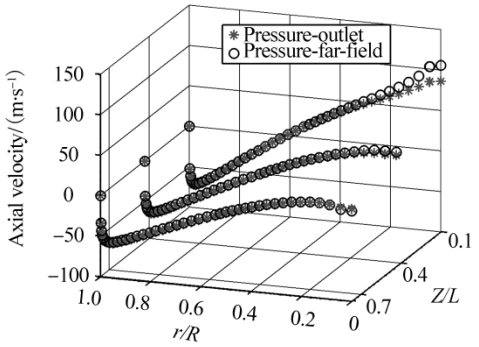

Fig. 9 Comparison of axial velocities at different longitudinal sections for two different boundary conditions

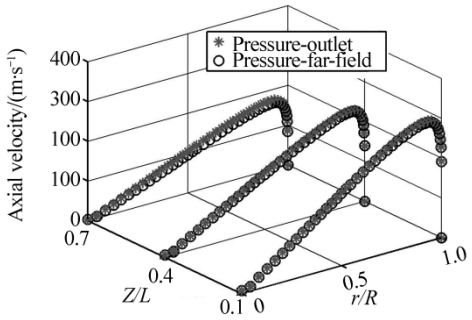

Fig. 10 Comparison of tangential velocities at different longitudinal sections for two different boundary conditions

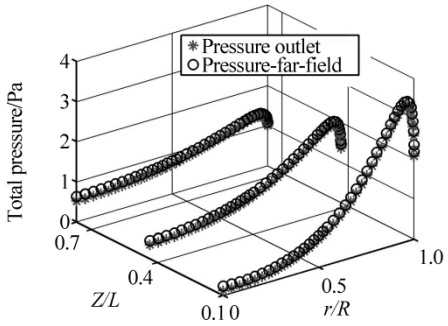

Fig. 11 Comparison of total pressures at different longitudinal sections for two different boundary conditions

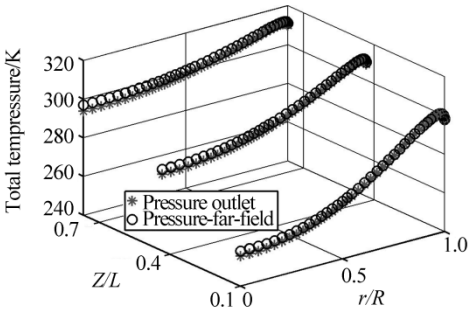

Fig. 12 Comparison of total temperatures at different longitudinal sections for two different boundary conditions

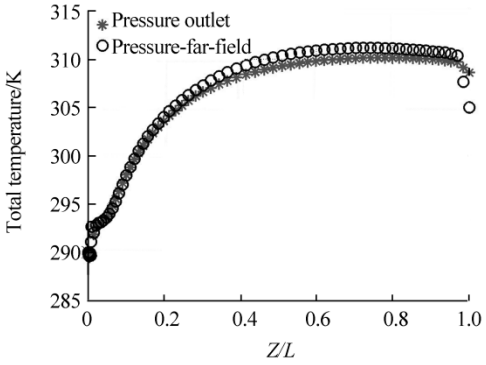

Fig. 13 Indication of total temperature on wall of main tube for two different boundary conditions

4 Results of effect of different operating gases

In the present study, the thermal performance of the air separator for cold and hot exhaust temperatures (T_c and T_h) is analyzed, and the cold and hot power separation rates ($\dot{Q}_c$ and $\dot{Q}_h$) are predicted numerically. These predictions are based on different operating gases used as operating fluids, as previously referred to. The resulting total temperature contours are plotted in Fig. 14, where it is possible to see the cold core and hot peripheral flow along the main tube of the vortex tube air separator. It is assumed that the inlet mass flow rate is 8.34 g/s, inlet temperature is 294.2 K, and that air is the working fluid; minimum and maximum total temperatures produced under these operating conditions are 250.24 and 311.5 K, respectively. The total temperature contour plotted in Fig. 14 is based on α=0.3 (optimum cold flow fraction), which means that the machine produces the maximum cooling capacity using this cold flow fraction.

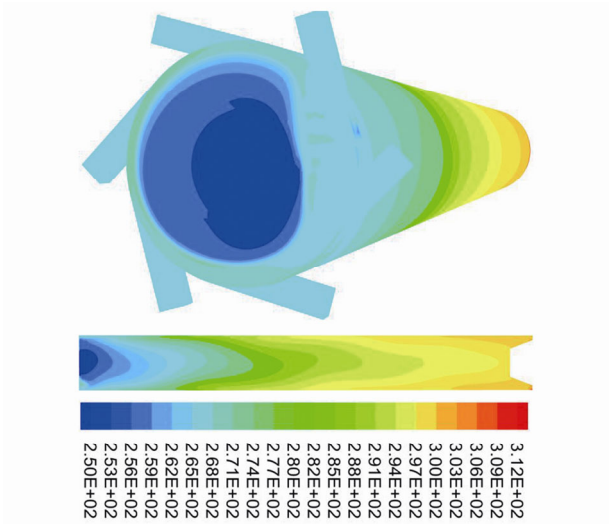

Fig. 14 Temperature distribution in vortex tube operating with compressed air, α=0.3

The main objective of this investigation is to determine the maximum cooling and heating capacities obtained using

different operating gases, as this controls the rate of energy separation in the commercial vortex tube. Fig. 15 presents variations of cold temperature measured at the exhaust of the cold orifice as a function of the cold flow fraction, where the trend of the experimental curve shows that the temperature of the cold exit increases with an increasing cold flow fraction (for cold flow fraction values greater than 0.36). In the case of air, there is a favorable agreement between the experimental results and CFD outputs, which proves that the 3D CFD model is an accurate and reliable model for use in predicting the thermal performance of the vortex tube air separator. This numerical model is then used to analyze and predict energy and gas separation in the air separator using other operating gases, including NO_2, CO_2, N_2, and O_2. As shown in the results of Fig. 15, all of these gases produce a lower cold temperature than air, and thus the use of these operating gases instead of air leads to a higher cooling efficiency. For example, the cold exhaust temperature for air as the operating gas is 252.2 K, and when N_2 or CO_2 is injected into the air separator the cold temperature reduces by approximately 3 or 9 K, respectively (for α=0.37). Fig. 15 indicates that the minimum possible cold temperature of the vortex tube is associated with the use of NO_2 for α=0.37, which is equal to 240.73 K.

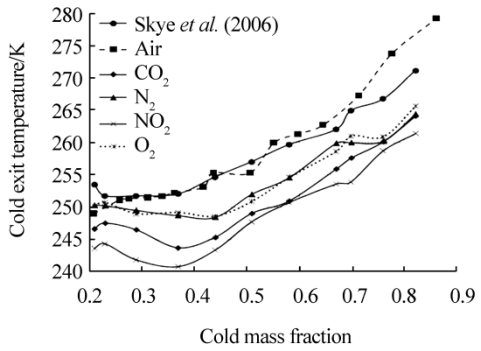

Fig. 15 Variation of cold exhaust temperature for different types of operating gases as a function of cold flow fraction (compared with experimental results)

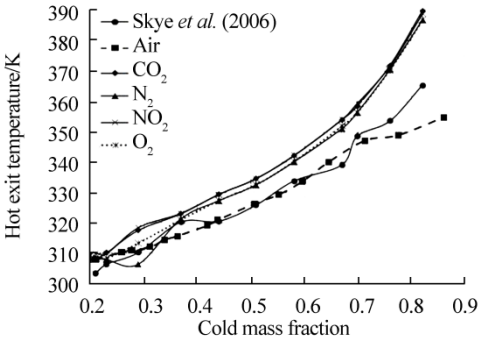

Fig. 16 Variation in hot exhaust temperature for different types of operating gasesas a function of cold flow fraction (compared with experimental results)

This prediction emphasizes that when the vortex tube air separator is utilized as a refrigerator system, NO_2 is the best choice out of all the above-mentioned gases because it produces a lower temperature than these other gases. The minimum value of the cold exit temperature for all gases exists in the cold flow fraction range of 0.29–0.37. Fig. 16 shows the behavior of temperature curves in relation to hot gases that escape from the hot exhaust (as a function of the cold mass fraction). As shown in Fig. 16, the various different gases have the same general tendency at the hot exit at different cold flow factions, and in all models the hot exit temperature is enhanced with an increase in the cold flow fraction. Fig. 16 also indicates that if the vortex tube air separator is used as a heating system, the effect of using any of the mentioned gases would be the same (excluding air). Therefore, it is possible to choose the cheapest gas because there is no difference between the effect of the gases from a heating perspective. In the case of air, the experimental and numerical hot temperatures are in perfect agreement, and it is therefore possible to trust the CFD model to predict both hot temperatures and the cold exit temperature. The hot gases temperatures (NO_2, CO_2, N_2, and O_2) that exit from the hot exhaust range between 309.89 and 388.86 K. Table 2 summarizes the numerical results of hot and cold exhaust temperatures (T_c and T_h) and their differences (ΔT_c and ΔT_h) for all types of operating gases at a cold flow fraction of α=0.3. Results show that out of all gases investigated, the maximum amounts of ΔT_c=53.12 K and ΔT_h=24.13 K are achieved for NO_2.

Table 2 Numerical temperature separation for different operating gases at cold mass fraction of α=0.3 K

Type of gas	Cold exhaust temperature	Hot exhaust temperature	ΔT_c	ΔT_h	ΔT_t
Air	250.24	311.5	43.96	17.3	61.26
CO_2	246.48	317.5	47.72	23.3	71.02
N_2	249.48	306.42	44.72	12.22	56.94
NO_2	241.08	318.33	53.12	24.13	77.25
O_2	248.95	313.28	45.25	19.08	64.33

Table 3 Order of cooling and heating capabilities for differing operating gases

Cooling preference	Heating preference
NO_2	NO_2
CO_2	CO_2
O_2	O_2
N_2	Air
Air	N_2

Table 3 offers a practical suggestion for determining the type of operating gas to achieve maximum cooling or heating power. Within the table, gases with higher heating (ΔT_h) and cooling (ΔT_c) abilities are arranged in order from top to bottom. However, from an economic standpoint, it appears that air is more appropriate and affordable for use in

the vortex tube air separator system because of its unlimited and free access, although other operating gases have higher cooling and heating capabilities but involve higher costs.

Another parameter used to illustrate the air separator's performance is that of the energy separation rate at hot and cold exits ($\dot{Q}_c$ and $\dot{Q}_h$), which can be evaluated as follows:

$$\dot{Q}_c = \dot{m}_c c_p (T_i - T_c) \tag{15}$$

$$\dot{Q}_h = \dot{m}_h c_p (T_h - T_i) \tag{16}$$

where the term c_p, is the gas specific heat.

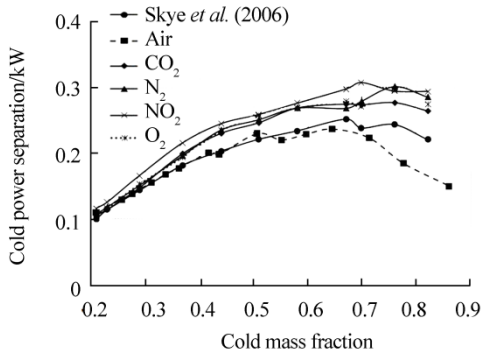

Fig. 17 Variation in cold power separation between the different types of operating gases as a function of cold flow fraction (compared with experimental results)

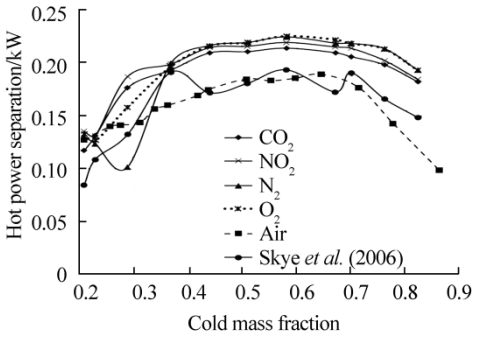

Fig. 18 Variation in hot power separation between the different types of operating gases as a function of cold flow fraction (compared with experimental results)

Figs. 17 and 18 show variations in cold and hot power separation ($\dot{Q}_c$ and $\dot{Q}_h$) for the vortex tube air separator using various operating gases (in comparison with experimental values). Both the experimental results and CFD models show that maximum power separation occurs at a cold fraction of about 0.65, and that the rate of energy separation is enhanced with an increased cold flow fraction in the range of 0.21–0.65. For cold flow fraction values greater than 0.7 there is no increasing trend in power separation, and the thermal rates decreases with an increase in the cold flow fraction. It appears that the molar mass of the mentioned gases (air, N_2, O_2, CO_2, and NO_2) has a very important role in the energy separation process in the vortex tube, and a higher molar mass value leads to the higher rate of energy separation. For example, NO_2 has the highest molar mass (46 g/mol) and creates the maximum cooling and heating power separation, followed by CO_2 with a molar mass value of 44.01 g/mol, and then O_2 and N_2 with molar mass values of 31.99 and 28.01 g/mol, respectively.

5 Conclusions

In this study, a 3D CFD model was improved by investigating thermal and gas separation in a vortex tube air separator, with the aim of developing a predictive tool. The developed 3D numerical model is restricted by the following considerations: (a) the operating fluid properties are constant; (b) the flow field regime is assumed to be fully turbulent; (c) and the steady-state condition is considered. A commercial code (Fluent 6.3.26) was employed to simulate turbulent patterns in the air separator using the standard k–ε turbulence model. The main objective of the research was to study the effects of using different gases (as the operating fluids) on the cooling and heating capabilities of an air separator. It is considered that the results of this study will help researchers select the best type of the operating gas for a vortex tube air separator to achieve the highest cooling and heating capabilities. Our study found that NO_2 is the best choice for cooling or heating a special zone by the means of the vortex tube air separator, and it creates colder and warmer streams simultaneously to produce the maximum cooling and heating performance in comparison with the use of other gases. In this study, a comprehensive comparison between two different types of boundary conditions for hot and the cold exhausts was performed, i.e., the pressure-far-field and pressure-outlet. If pressure values at the cold and hot exhausts are measured in experiments, it is possible for researchers to use the pressure-outlet boundary condition to perform computations, and thus this method is applicable for use when access to laboratory data is possible. However, in this study, we introduce a boundary condition method for use by researchers who do not have access to laboratory data and thus introduce a simple way to analyze a real model of an air separator without any knowledge of the pressure values at exhausts. This is possible because pressure values are not required when the model is designed based on the pressure-far-field boundary condition. A comparison between the present numerical results and the available measured experimental data revealed good and reliable agreement.

References

Baghdad M, Ouadha A, Imine O, Addad Y, 2011. Numerical study of energy separation in a vortex tube with different RANS models. *International Journal of Thermal Sciences*, **50**(12), 2377-2385.
DOI: 10.1016/j.ijthermalsci.2011.07.011

Bovand M, Valipour MS, Dincer K, Tamayol A, 2014a. Numerical analysis of the curvature effects on Ranque–Hilsch vortex tube refrigerators. *Applied Thermal Engineering*, **65**(1-2), 176-183. DOI: 10.1016/j.applthermaleng.2013.11.045

Bovand M, Valipour MS, Eiamsa-ard S, Tamayol A, 2014b. Numerical analysis for curved vortex tube optimization. *International Communications in Heat and Mass Transfer*, **50**, 98-107. DOI: 10.1016/j.icheatmasstransfer.2013.11.012

Dincer K, 2011. Experimental investigation of the effects of threefold type Ranque–Hilsch vortex tube and six cascade type Ranque–Hilsch vortex tube on the performance of counter flow Ranque–Hilsch vortex tubes. *International Journal of Refrigeration*, **34**(6), 1366-1371. DOI: 10.1016/j.ijrefrig.2011.05.008

Dutta T, Sinhamahapatra KP, Bandyopadhyay SS, 2011. Numerical investigation of gas species and energy separation in the Ranque–Hilsch vortex tube using real gas model. *International Journal of Refrigeration*, **26**(8), 2118-2128. DOI: 10.1016/j.ijrefrig.2011.06.004

Han X, Li N, Wu K, Wang Z, Tang L, Chen G, Xu X, 2013. The influence of working gas characteristics on energy separation of vortex tube. *Applied Thermal Engineering*, **61**(2), 171-177. DOI: 10.1016/j.applthermaleng.2013.07.027

Hilsch R, 1947. The use of expansion of gases in a centrifugal field as a cooling process. *Review of Scientific Instruments*, **18**, 108-113.

Im SY, Yu SS, 2012. Effects of geometric parameters on the separated air flow temperature of a vortex tube for design optimization. *Energy*, **37**(1), 154-160. DOI: 10.1016/j.energy.2011.09.008

Mohammadi S, Farhadi F, 2013. Experimental analysis of a Ranque–Hilsch vortex tube for optimizing nozzle numbers and diameter. *Applied Thermal Engineering*, **61**(2), 500-506. DOI: 10.1016/j.applthermaleng.2013.07.043

Pourmahmoud N, Hasanzadeh A, Rafiee SE, Rahimi M, 2012. Three dimensional numerical investigation of effect of convergent nozzles on the energy separation in a vortex tube. *International Journal of Heat and Technology*, **30**(2), 133-140.

Pourmahmoud N, Rafiee SE, Rahimi M, Hasanzadeh A, 2013. Numerical energy separation analysis on the commercial Ranque-Hilsch vortex tube on basis of application of different gases. *Scientia Iranica*, **20**(5), 1528-1537.

Pourmahmoud N, Rahimi M, Rafiee SE, Hasanzadeh A, 2014. A numerical simulation of the effect of inlet gas temperature on the energy separation in a vortex tube. *Journal of Engineering Science and Technology*, **9**(1), 81-96.

Rafiee SE, Ayenehpour S, Sadeghiazad MM, 2016. A study on the optimization of the angle of curvature for a Ranque–Hilsch vortex tube, using both experimental and full Reynolds stress turbulence numerical modelling. *Heat and Mass Transfer*, **52**(2), 337-350. DOI: 10.1007/s00231-015-1562-y

Rafiee SE, Rahimi M, 2013. Experimental study and three-dimensional (3D) computational fluid dynamics (CFD) analysis on the effect of the convergence ratio, pressure inlet and number of nozzle intake on vortex tube performance-Validation and CFD optimization. *Energy*, **63**, 195-204. DOI: 10.1016/j.energy.2013.09.060

Rafiee SE, Rahimi M, 2014.Three-dimensional simulation of fluid flow and energy separation inside a vortex tube. *Journal of Thermophysics and Heat Transfer*, **28**, 87-99. DOI: 10.2514/1.T4198

Rafiee SE, Rahimi M, Pourmahmoud N, 2013. Three-dimensional numerical investigation on a commercial vortex tube based on an experimental model-Part I: Optimization of the working tube radius. *International Journal of Heat and Technology*, **31**(1), 49-56.

Rafiee SE, Sadeghiazad MM, 2014a. Three-dimensional and experimental investigation on the effect of cone length of throttle valve on thermal performance of a vortex tube using k–ε turbulence model. *Applied Thermal Engineering*, **66**(1-2), 65-74.

Rafiee SE, Sadeghiazad MM, 2014b. Effect of conical valve angle on cold-exit temperature of vortex tube. *Journal of Thermophysics and Heat Transfer*, **28**(4), 785-794. DOI: 10.2514/1.T4376

Rafiee SE, Sadeghiazad MM, 2014c. 3D CFD exergy analysis of the performance of a counter flow vortex tube. *International Journal of Heat and Technology*, **32**(1-2), 71-77.

Rafiee SE, Sadeghiazad MM, 2015. 3D numerical analysis on the effect of rounding off edge radius on thermal separation inside a vortex tube. *International Journal of Heat and Technology*, **33**(1), 83-90.

Rafiee SE, Sadeghiazad MM, 2016. Three-dimensional computational prediction of vortex separation phenomenon inside Ranque-Hilsch vortex tube. *Aviation*, **20**(1), 21-31. DOI: 10.3846/16487788.2016.1139814

Rafiee SE, Sadeghiazad MM, Mostafavinia N, 2015. Experimental and numerical investigation on effect of convergent angle and cold orifice diameter on thermal performance of convergent vortex tube. *Journal of Thermal Science and Engineering Applications*, **7**(4), 041006. DOI: 10.1115/1.4030639

Rahimi M, Rafiee SE, Pourmahmoud N, 2013. Numerical investigation of the effect of divergent hot tube on the energy separation in a vortex tube. *International Journal of Heat and Technology*, **31**(2), 17-26.

Ranque GJ, 1933. Experiments on expansion in a vortex with simultaneous exhaust of hot air and cold air. *Le Journal de Physique et le Radium*, **4**, 112-114.

Shamsoddini R, Hossein Nezhad A, 2010. Numerical analysis of the effects of nozzles number on the flow and power of cooling of a vortex tube. *International Journal of Refrigeration*, **33**(4), 774-782. DOI: 10.1016/j.ijrefrig.2009.12.029

Skye HM, Nellis GF, Klein, SA, 2006. Comparison of CFD analysis to empirical data in a commercial vortex tube. *International Journal of Refrigeration*, **29**, 71-80.

Thakare HR, Parekh AD, 2015. Computational analysis of energy separation in counter—flow vortex tube. *Energy*, **85**, 62-77. DOI: 10.1016/j.energy.2015.03.058

Valipour MS, Niazi N, 2011. Experimental modeling of a curved Ranque-Hilsch vortex tube refrigerator. *International Journal of Refrigeration*, **34**, 1109-1116.

Xue Y, Arjomandi M, Kelso R, 2013a. Energy analysis within a vortex tube. *Experimental Thermal and Fluid Science*, **52**, 139-145. DOI: 10.1016/j.expthermflusci.2013.09.004

Xue Y, Arjomandi M, Kelso R, 2013b. Experimental study of the thermal separation in a vortex tube. *Experimental Thermal and Fluid Science*, **46**, 175-182. DOI: 10.1016/j.expthermflusci.2012.12.009